Complementary Thermodynamic Mechanisms of Boron and Carbon Segregation at Grain Boundaries in Nickel Alloys

Tyler D. Doležal*[1,2], Rodrigo Freitas*[1], and Ju Li*[1,3]

[1]Department of Materials Science and Engineering, Massachusetts Institute of Technology, Cambridge, MA, USA
[2]Department of Engineering Physics, Air Force Institute of Technology, Wright-Patterson Air Force Base, OH, USA
[3]Department of Nuclear Science and Engineering, Massachusetts Institute of Technology, Cambridge, MA, USA

March 28, 2026

*corresponding authors: dolez120@mit.edu; rodrigof@mit.edu; liju@mit.edu

1 Simulation Cells

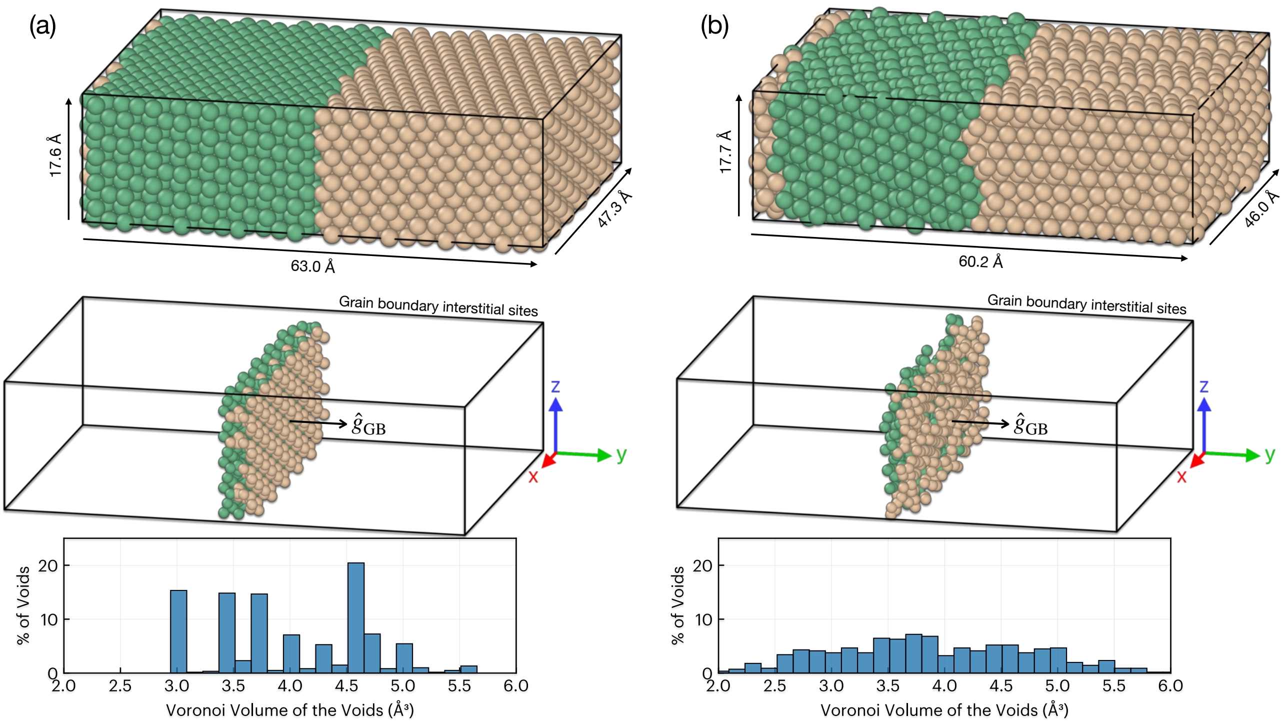

Figure S1: (a) The undoped pure Ni $\Sigma5\,[001]\,(210)$ symmetric tilt (S5) grain boundary and (b) custom-built high-angle (HA) grain boundary, both visualized in OVITO [1] with the grain segmentation modifier applied. The panels below each structure show the distribution of pre-identified interstitial void sites along the grain boundary. The corresponding histograms reveal that the S5 boundary exhibits a narrow, well-defined void size distribution, whereas the HA boundary displays a broader and more irregular distribution, indicative of higher structural disorder and greater variability in available interstitial volumes.

Fig. S1 shows schematics of the two grain boundary structures and their void distribution used for this study. The calculated grain boundary energies for the undoped pure Ni reference structures were 1.20 $\mathrm{J\,m^{-2}}$ for S5 and 1.74 $\mathrm{J\,m^{-2}}$ for HA.

2 Custom-built Grain Boundary

Several pure Ni bicrystal grain boundary structures ($\mathrm{Fm\bar{3}m}$ cubic system) were generated with random orientations using Atomsk [2]. To optimize the highly misoriented configurations, a vacancy-driven relaxation procedure was employed: one Ni atom was iteratively removed from the grain boundary core, followed by conjugate-gradient (CG) relaxation with a force tolerance of 0.01 eV/Å using LAMMPS [3]. Structures were recorded after each deletion step, and the process was repeated until the grain boundary energy (γ_{GB}) converged (Fig. S2). The grain boundary energy was computed as

$$\gamma_{\mathrm{GB}} = \frac{E - N\left(E_{\mathrm{bulk}}/N_{\mathrm{bulk}}\right)}{2A_{\mathrm{GB}}}, \tag{S-1}$$

where E is the total energy of the grain boundary system containing N atoms, E_{bulk} is the total energy of the bulk reference cell with N_{bulk} atoms, and A_{GB} is the area of a single grain boundary. The final selected structure was annealed at 1000 K for 40 ps under canonical (NVT)

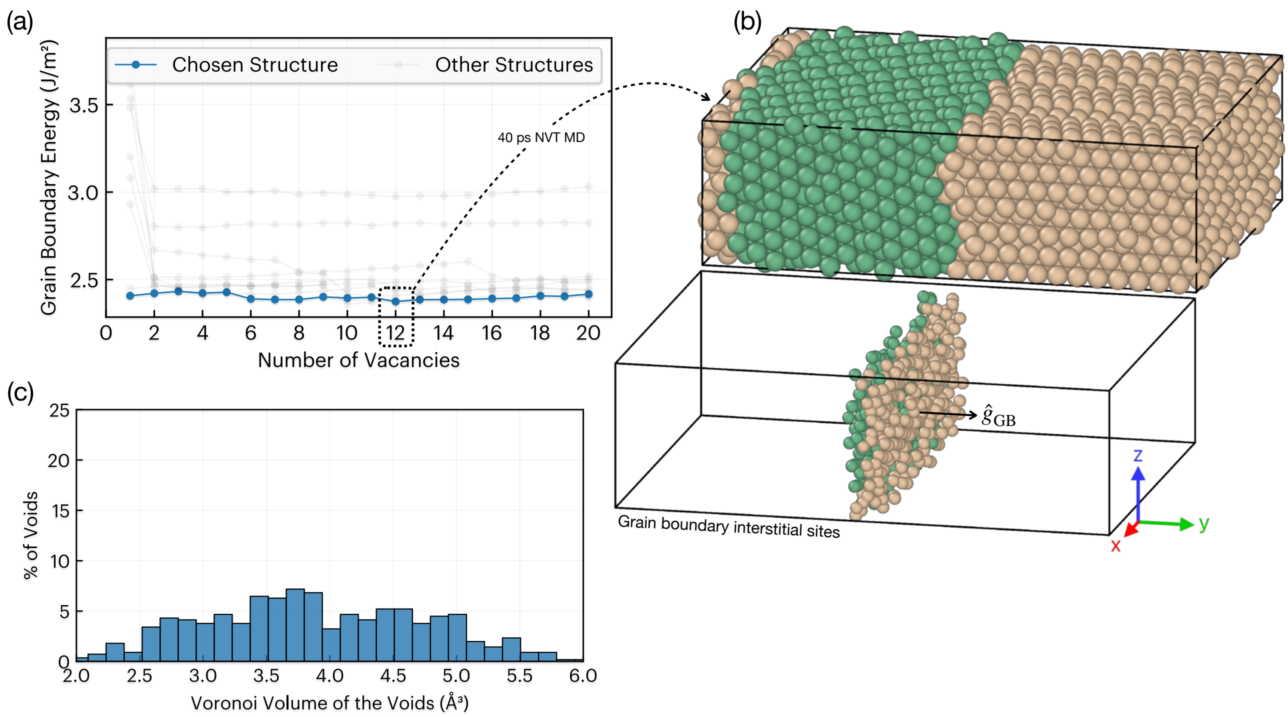

Figure S2: (a) Grain boundary energies of pure Ni for a series of randomly generated, highly misoriented bicrystals, plotted as a function of iterative atomic deletions from the grain boundary core. Black curves represent alternative configurations, while the blue curve highlights the trajectory of the selected structure. (b) Post-annealed configuration of the chosen grain boundary, visualized with the grain segmentation modifier in OVITO [1]. The lower panel identifies pre-determined interstitial void sites targeted for subsequent hybrid semi-grand canonical/grand canonical Monte Carlo simulations. (c) Histogram of the Voronoi volumes associated with the pre-determined void sites in the custom-built grain boundary, illustrating a broad distribution of accessible interstitial motifs.

conditions using a timestep of 1 fs. The chosen high-angle grain boundary corresponds to a non-CSL boundary with a misorientation angle of 106.5°.

3 Semi-Grand Canonical $\Delta\mu$ Data

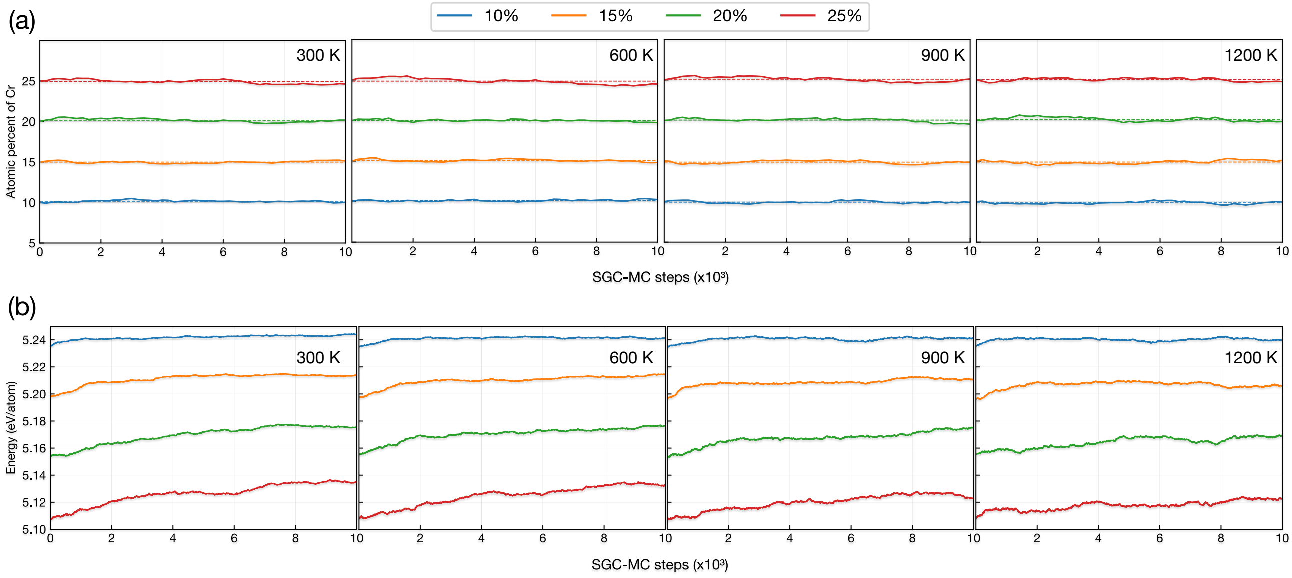

Figure S3: (a) Evolution of the Cr atomic percent during semi-grand canonical Monte Carlo (SGC–MC) simulations performed with the final calibrated $\Delta\mu_{\mathrm{Cr}\to\mathrm{Ni}}$ values in the $10 \times 10 \times 10$ bulk FCC simulation cell. Dashed lines indicate the mean x_{Cr} achieved over each run. (b) Corresponding absolute total energy per atom as a function of MC step.

$\Delta\mu$ Convergence. To efficiently determine the transmutation chemical potentials ($\Delta\mu_{\mathrm{Cr}\to\mathrm{Ni}}$) for Ni–Cr alloys, we employed a two-stage semi-grand canonical Monte Carlo (SGC-MC) convergence procedure. Initial convergence scans were performed on $7 \times 7 \times 7$ FCC bulk supercells ($n = 1372$ atoms), which were initialized at the target Cr composition $x_{\mathrm{Cr}}^{(\mathrm{tgt})}$ and equilibrated for 10^4 Monte Carlo steps. In this first stage, $\Delta\mu_{\mathrm{Cr}\to\mathrm{Ni}}$ was varied in increments of approximately 0.01–0.05 eV until the equilibrium composition $\langle x_{\mathrm{Cr}} \rangle$ converged to within ± 0.2 at.% of the target value. These small-cell calculations enabled rapid, coarse-grained exploration of the appropriate $\Delta\mu_{\mathrm{Cr}\to\mathrm{Ni}}$ range.

The refined $\Delta\mu_{\mathrm{Cr}\to\mathrm{Ni}}$ values were then transferred to larger $10 \times 10 \times 10$ FCC supercells ($n = 4000$ atoms), again initialized at $x_{\mathrm{Cr}}^{(\mathrm{tgt})}$ and equilibrated for 10^4 Monte Carlo steps. At this larger size, fine adjustments on the order of 0.001–0.005 eV were sufficient to converge $\langle x_{\mathrm{Cr}} \rangle$ to within ± 0.2 at.% of the target composition. This hierarchical approach ensured that coarse errors were eliminated quickly in smaller systems, while final convergence accuracy was established in statistically smoother larger systems.

The statistical justification for this two-stage procedure follows from the variance of concentration fluctuations in a semi-grand canonical ensemble. For a binary system of N substitutional sites with composition $x = N_{\mathrm{Cr}}/N$, small fluctuations around the equilibrium mean $\langle x \rangle$ satisfy

$$\sigma_x^2 = \frac{\langle (\delta N_{\mathrm{Cr}})^2 \rangle}{N^2} = \frac{\chi}{N}, \tag{S-2}$$

where χ is the chemical susceptibility associated with the alloy free-energy curvature. Thus, the standard deviation of the instantaneous composition scales as

$$\sigma_x \propto \frac{1}{\sqrt{N}}. \tag{S-3}$$

Since the transmutation chemical potential difference is related to the derivative of the free energy with respect to composition,

$$\Delta\mu = \frac{1}{N}\left(\frac{\partial G}{\partial x}\right)_{T,P,N}, \tag{S-4}$$

the finite-size sensitivity of $\Delta\mu$ to discrete changes in x introduces an additional factor of $1/N$ in the effective numerical resolution. Consequently, the statistical uncertainty in $\Delta\mu$ scales as

$$\sigma_{\Delta\mu} \propto \frac{1}{\sqrt{N}}, \tag{S-5}$$

while the discretization (finite-size) error decreases more rapidly, as $\mathcal{O}(1/N)$. This behavior explains why smaller supercells are sufficient for rapid coarse-grained exploration of $\Delta\mu_{\mathrm{Cr}\to\mathrm{Ni}}$, whereas larger supercells provide the necessary statistical precision for final convergence. The final values for $\Delta\mu_{\mathrm{Cr}\to\mathrm{Ni}}$ are compiled in Table S1.

x_{Cr} (at.%)	300 K	600 K	900 K	1200 K
10	0.511	0.494	0.461	0.416
15	0.642	0.634	0.603	0.581
20	0.800	0.779	0.770	0.739
25	0.936	0.915	0.901	0.870

Table S1: Calculated $\Delta\mu_{\mathrm{Cr}\to\mathrm{Ni}}$ (eV) as a function of Cr composition x_{Cr} and temperature T, obtained from SGC-MC simulations.

$\Delta\mu$ Linear Fitting. At moderate substitutional solute concentrations, the excess free energy of mixing per site (G/N) for binary alloys can be described within the regular solution model as

$$G_{\mathrm{mix}}(x_{\mathrm{Cr}}, T) = \Omega\, x_{\mathrm{Cr}}(1 - x_{\mathrm{Cr}}) + k_{\mathrm{B}}T\,[x_{\mathrm{Cr}} \ln x_{\mathrm{Cr}} + (1 - x_{\mathrm{Cr}}) \ln(1 - x_{\mathrm{Cr}})], \tag{S-6}$$

where Ω is the regular solution interaction parameter representing the enthalpy of mixing. The transmutation chemical potential difference between Cr and Ni is obtained from the derivative of G_{mix} with respect to composition at fixed temperature and pressure,

$$\left(\frac{\partial G_{\mathrm{mix}}}{\partial x_{\mathrm{Cr}}}\right)_{T,P} = \Delta\mu_{\mathrm{Cr}\to\mathrm{Ni}}(x_{\mathrm{Cr}}, T) = \Omega(1 - 2x_{\mathrm{Cr}}) + k_{\mathrm{B}}T \ln\left(\frac{x_{\mathrm{Cr}}}{1 - x_{\mathrm{Cr}}}\right). \tag{S-7}$$

For the moderate composition range considered here (10-25 at.%), both terms in Eq. (S-7) vary nearly linearly with x_{Cr}, as the logarithmic term can be expanded about a representative composition $x_0 \in (0, 1)$:

$$\ln\left(\frac{x_{\mathrm{Cr}}}{1 - x_{\mathrm{Cr}}}\right) \approx \ln\left(\frac{x_0}{1 - x_0}\right) + \frac{x_{\mathrm{Cr}} - x_0}{x_0(1 - x_0)}. \tag{S-8}$$

Substituting this approximation into Eq. (S-7) yields a first-order relation of the form

$$\Delta\mu_{\mathrm{Cr}\to\mathrm{Ni}}(x_{\mathrm{Cr}}, T) \simeq A(T) + B(T)\, x_{\mathrm{Cr}}, \tag{S-9}$$

where the coefficients $A(T)$ and $B(T)$ are defined as

$$A(T) = \Omega + k_{\mathrm{B}}T \ln\left(\frac{x_0}{1 - x_0}\right) - \frac{k_{\mathrm{B}}T\, x_0}{1 - x_0}, \tag{S-10}$$

$$B(T) = -2\Omega + \frac{k_{\mathrm{B}}T}{x_0(1 - x_0)}. \tag{S-11}$$

Here, $A(T)$ collects the constant and entropic offset terms, while $B(T)$ captures the combined enthalpic and entropic dependence on composition.

Starting from Eq. (S-9) we treat the temperature dependence of the coefficients as smooth over the range considered and expand each to first order in T:

$$A(T) \approx A_0 + A_1 T, \qquad B(T) \approx B_0 + B_1 T, \tag{S-12}$$

where A_0, A_1, B_0, B_1 are T-independent constants (local expansion coefficients). Substituting Eq. (S-12) into Eq. (S-9) gives

$$\begin{aligned}\Delta\mu(x_{\mathrm{Cr}}, T) &\approx (A_0 + A_1 T) + (B_0 + B_1 T)\, x_{\mathrm{Cr}} \\ &= \underbrace{A_0}_{a_0} + \underbrace{B_0}_{a_1}\, x_{\mathrm{Cr}} + \underbrace{A_1}_{a_2}\, T + \underbrace{B_1}_{a_3}\, x_{\mathrm{Cr}} T.\end{aligned} \tag{S-13}$$

Equation (S-13) is the most general first-order (in x_{Cr} and T) form and contains a possible interaction term $a_3 x_{\mathrm{Cr}} T$ arising from the T-dependence of $B(T)$. In this work we adopt the final model of Eq. (S-14),

$$\Delta\mu_{\mathrm{Cr}\to\mathrm{Ni}}(x_{\mathrm{Cr}}, T) \approx a_0 + a_1\, x_{\mathrm{Cr}} + a_2\, T + a_3\, x_{\mathrm{Cr}}\, T. \tag{S-14}$$

The regression coefficients listed in Table S2 reproduce the simulated data with a root-mean-square error of 0.0079 eV. A parity plot comparing predicted and simulated values is shown in Fig. S4. The positive value of a_3 indicates that the sensitivity of $\Delta\mu_{\mathrm{Cr}\to\mathrm{Ni}}$ to Cr composition increases with temperature, consistent with a mild entropic enhancement of solute activity. The overall temperature slope, governed by a_2, remains negative, signifying a reduction in the Cr-to-Ni driving potential with increasing T. Together, these trends suggest that the effective chemical potential difference becomes less compositionally uniform at elevated temperature, a behavior aligned with thermally activated short-range order fluctuations in the Ni–Cr solid solution.

Parameter	Value
a_0 (eV)	0.2673
a_1 (eV)	2.7540
a_2 (10^{-4} eV K^{-1})	−1.177
a_3 (10^{-4} eV K^{-1})	2.267

Table S2: Eq. (S-14) coefficients.

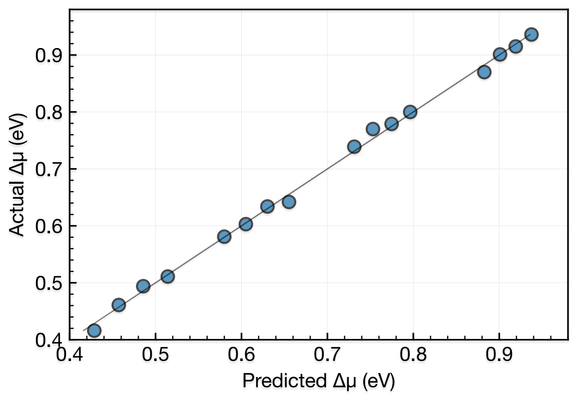

Figure S4: Parity plot comparing predicted and simulated $\Delta\mu_{\mathrm{Cr}\to\mathrm{Ni}}$ values from Eq. (S-14).

Uncovering Ω. A direct route to recover Ω from the fitted coefficients is obtained by matching the partial derivatives of $\Delta\mu_{\mathrm{Cr}\to\mathrm{Ni}}$ as given in Eqs. (S-7) and (S-14). Taking $\partial/\partial T$ of Eq. (S-7) at fixed x_{Cr} gives

$$\left(\frac{\partial \Delta\mu}{\partial T}\right)_x = k_{\mathrm{B}} \ln\left(\frac{x}{1-x}\right), \tag{S-15}$$

while from Eq. (S-14),

$$\left(\frac{\partial \Delta\mu}{\partial T}\right)_x \approx a_2 + a_3\, x_{\mathrm{Cr}}. \tag{S-16}$$

We define the anchor composition $x_0 \in (0,1)$ by equating Eqs. (S-15) and (S-16):

$$a_2 + a_3 x_0 \approx k_{\mathrm{B}} \ln\left(\frac{x_0}{1-x_0}\right). \tag{S-17}$$

Eq. (S-17) is solved once (numerically) for the fitted (a_2, a_3) and k_{B}; yielding

$$x_0 \approx 0.463. \tag{S-18}$$

The anchor composition x_0 lies outside our simulation range as it represents the composition at which the temperature dependence of the fitted model $(\partial\Delta\mu/\partial T)|_x = a_2 + a_3 x$ matches that predicted by regular solution theory. This thermodynamic consistency condition ensures that the bilinear interpolation correctly captures the entropic contribution to $\Delta\mu$ across the temperature range 300–1200 K.

The maximum deviation of the linearization in Eq. (S-8) from the exact logarithm over the range $x_{\mathrm{Cr}} \in [0.10, 0.25]$ is

$$\varepsilon_{\log} = \max_{x\in[0.10,0.25]} \left| \ln\left(\frac{x}{1-x}\right) - \left[\ln\left(\frac{x_0}{1-x_0}\right) + \frac{x-x_0}{x_0(1-x_0)}\right]\right| \approx 0.092. \tag{S-19}$$

At 300 K, this corresponds to an energy error of $k_B T \cdot \varepsilon_{\log} \approx 0.0024$ eV, which is negligible compared to the total variation in $\Delta\mu_{\mathrm{Cr}\to\mathrm{Ni}}$ ($\sim$0.4 eV across the composition range) and below the RMSE of the full bilinear fit (0.0079 eV). At 1200 K, the error scales to $\sim$0.010 eV, still within our target convergence tolerance of $\pm$0.01 eV. These values confirm that the linearization introduces errors smaller than the statistical uncertainty of the SGC-MC simulations.

Continuing on, taking $\partial/\partial x$ of Eq. (S-7) at fixed T gives

$$\left(\frac{\partial \Delta\mu}{\partial x}\right)_T = -2\Omega + \frac{k_{\mathrm{B}} T}{x(1-x)}, \tag{S-20}$$

while from Eq. (S-14),

$$\left(\frac{\partial \Delta\mu}{\partial x}\right)_T \approx a_1 + a_3\, T. \tag{S-21}$$

Equating Eqs. (S-20) and (S-21) at the representative composition x_0 yields

$$a_1 + a_3 T \approx -2\Omega(T) + \frac{k_{\mathrm{B}} T}{x_0(1-x_0)} \quad \Longrightarrow \quad \boxed{\Omega(T) \approx \tfrac{1}{2}\left[\frac{k_{\mathrm{B}} T}{x_0(1-x_0)} - (a_1 + a_3 T)\right].} \tag{S-22}$$

The resulting $\Omega(T)$ values are summarized in Table S3. The inclusion of the $a_3 x_{\mathrm{Cr}} T$ term slightly moderates the temperature dependence of $\Omega(T)$, reflecting the weak but measurable coupling between solute concentration and thermal excitation. Negative Ω values indicate exothermic mixing, consistent with the random substitutional solid-solution behavior of the Ni–Cr system over the temperature range considered [4].

4 Derivation of Interstitial Concentration Expression

Conceptual framework. Interstitial atoms (e.g., B or C) are treated as dilute point defects, analogous to vacancies except that they occupy non-lattice sites rather than vacating lattice

	T (K)			
	300	600	900	1200
$\Omega(T)$ (eV)	−1.359	−1.341	−1.323	−1.305

Table S3: Temperature-dependent regular solution interaction parameter $\Omega(T)$ computed from Eq. (S-22) using the coupled first-order fit coefficients in Table S2 and the anchor composition x_0 from Eq. (S-18).

sites. We consider an n-atom host alloy containing S substitutional species ($s = 1, \ldots, S$), such as Ni and Cr, defined on a single face-centered cubic (FCC) sublattice. The total number of host atoms is

$$N = \sum_{s=1}^{S} N_s, \tag{S-23}$$

and the total number of available interstitial sites is N_{int}. A small fraction N_I of these sites is occupied by interstitial atoms, such that $N_I \ll N_{\text{int}}$ in the dilute limit.

The Helmholtz free energy of the system is

$$F(N_1, \ldots, N_S, N_I; T) = -k_{\text{B}} T \ln Z, \tag{S-24}$$

where Z is the partition function of the alloy, including configurational and vibrational degrees of freedom. The corresponding chemical potentials are

$$\mu_s = \left(\frac{\partial F}{\partial N_s}\right)_{T,\{N_{s'\neq s}\},N_I}, \qquad \mu_I = \left(\frac{\partial F}{\partial N_I}\right)_{T,\{N_s\}}. \tag{S-25}$$

At thermodynamic equilibrium, the internal chemical potential of the interstitial species equals that of its external reservoir, $\mu_I = \mu_I^{\text{ext}}$, which may represent either a bulk reference state or a prescribed chemical potential chosen to achieve a target concentration.

Interstitial formation free energy. For an individual site j, the microscopic free-energy change associated with inserting one interstitial atom of species I is

$$\Delta f_I(\text{site } j) = -k_{\text{B}} T \ln \left[\frac{\displaystyle\int d(\delta q_N)\, e^{-U(s_N+\delta q_N;+\text{I@site } j)/k_{\text{B}}T}}{\displaystyle\int d(\delta q_N)\, e^{-U(s_N+\delta q_N)/k_{\text{B}}T}} \right], \tag{S-26}$$

where U is the potential energy and s_N denotes the underlying arrangement of substitutional atoms. The ensemble-averaged interstitial formation free energy is

$$\Delta f_I = \big\langle \Delta f_I(\text{site } j) \big\rangle_{s_N}. \tag{S-27}$$

In the limit of weak spectral dispersion (i.e., when insertion energies are narrowly distributed), we define a characteristic formation energy

$$E_I \equiv \big\langle \Delta f_I(\text{site } j) \big\rangle_{s_N} = \Delta f_I, \tag{S-28}$$

which simplifies the subsequent analysis by replacing the site-resolved distribution with a single representative value.

Equilibrium interstitial fraction. The equilibrium fraction of occupied interstitial sites can be obtained from a grand canonical Monte Carlo (GCMC) simulation in which all potential interstitial sites are equally sampled for insertion and deletion attempts. At equilibrium,

$$0 = \left(\frac{\partial G}{\partial N_I}\right)_{T,P,\{N_c\}} = \mu_I - \mu_I^{\text{ext}}, \tag{S-29}$$

with the Gibbs free energy $G = F + PV$ and μ_I^{ext} being the chemical potential of the external interstitial reservoir (a control parameter in GCMC simulations). The configurational entropy of dilute interstitials contributes a translational term

$$s_I^{\text{trans}} = -k_{\text{B}} \ln X_I, \qquad X_I \equiv \frac{N_I}{N_{\text{int}}} \ll 1. \tag{S-30}$$

The resulting equilibrium condition yields a Fermi–Dirac-like expression for the site occupancy $\theta_I \equiv X_I = N_I/N_{\text{int}},$,

$$\theta_I = \frac{1}{1 + \exp[(E_I - \mu_I^{\text{ext}})/k_{\text{B}}T]}, \tag{S-31}$$

which reduces in the dilute limit to the Boltzmann form

$$X_I^{\text{eq}}(T) \simeq \frac{1}{N_{\text{int}}} \left\langle \sum_{j=1}^{N_{\text{int}}} \exp\left[-\frac{\Delta f_I(\text{site } j) - \mu_I^{\text{ext}}}{k_{\text{B}}T}\right] \right\rangle. \tag{S-32}$$

Eq. (S-32) provides a practical estimator for the dilute interstitial fraction that (i) weights each potential site by its microscopic insertion free energy and (ii) naturally captures site-to-site spectrality through the exponential average. Sites with anomalously low $\Delta f_I(\text{site } j)$ dominate the average, consistent with the extreme-value statistics of rare, favorable traps.

Connection to mean site occupancy. Defining the mean occupancy as $\theta_I \equiv X_I^{\text{eq}} = N_I/N_{\text{int}}$, and assuming $\Delta f_I(\text{site } j)$ is narrowly distributed around a characteristic value E_I (weak spectrality), Eq. (S-32) reduces to

$$\theta_I \approx \frac{1}{1 + \exp\left[\frac{E_I - \mu_I^{\text{ext}}}{k_{\text{B}}T}\right]}. \tag{S-33}$$

In the dilute limit $\theta_I \ll 1$ (noninteracting interstitials),

$$\theta_I \approx \exp\left[-\frac{E_I - \mu_I^{\text{ext}}}{k_{\text{B}}T}\right]. \tag{S-34}$$

The dilute limit further implies negligible multi-interstitial interactions and non-overlapping strain fields, conditions under which the single-particle insertion approximation and Boltzmann weighting in Eq. (S-32) remain valid. In this regime, $E_I - \mu_I^{\text{ext}}$ may be either positive or weakly negative depending on the chemical potential of the external reservoir. When $\Delta f_I(\text{site } j)$ has finite spectral width, Eq. (S-32) can be written as a log-sum-exp over a site-energy density of states $p(\varepsilon)$:

$$\theta_I = \int d\varepsilon\, p(\varepsilon) \exp\left[-\frac{\varepsilon - \mu_I^{\text{ext}}}{k_{\text{B}}T}\right], \qquad \int p(\varepsilon)\, d\varepsilon = 1. \tag{S-35}$$

Equation (S-35) makes explicit that low-ε tails dominate θ_I, reflecting the physical role of rare, energetically favorable interstitial motifs.

Degeneracy and multiple interstitial sublattices. If there are m distinguishable interstitial sublattices (e.g., octahedral vs. tetrahedral) with site counts $\{N_{\mathrm{int}}^{(\alpha)}\}$ and formation energies $\{\Delta f_I^{(\alpha)}(j)\}$, Eq. (S-32) generalizes to

$$\theta_I = \frac{1}{\sum_\alpha N_{\mathrm{int}}^{(\alpha)}} \sum_{\alpha=1}^{m} \left\langle \sum_{j=1}^{N_{\mathrm{int}}^{(\alpha)}} \exp\left[-\frac{\Delta f_I^{(\alpha)}(j) - \mu_I^{\mathrm{ext}}}{k_{\mathrm{B}}T} \right] \right\rangle. \tag{S-36}$$

When one sublattice α^* is much more favorable (e.g., octahedral sites for B or C in FCC Ni), its contribution dominates Eq. (S-36), reducing the analysis to a single-manifold case.

For methodological transparency, it is convenient to define a composition-independent bulk reference E_0 as the insertion free energy of species I into a high-symmetry site (e.g., octahedral) of pure Ni at the same (T, P). If μ_{ext} is chosen to achieve a target bulk occupancy θ_{bulk} in this reference crystal, Eq. (S-33) gives

$$\theta_{\mathrm{bulk}} = \frac{1}{1 + \exp\left[\frac{E_0 - \mu_I^{\mathrm{ext}}}{k_{\mathrm{B}}T}\right]} \Longrightarrow \mu_I^{\mathrm{ext}} = E_0 + k_{\mathrm{B}}T \ln\left(\frac{\theta_{\mathrm{bulk}}}{1 - \theta_{\mathrm{bulk}}}\right). \tag{S-37}$$

In the dilute limit, $\theta_{\mathrm{bulk}} \ll 1$, Eq. (S-37) simplifies to

$$\mu_I^{\mathrm{ext}} \approx E_0 + k_{\mathrm{B}}T \ln \theta_{\mathrm{bulk}}. \tag{S-38}$$

Operationally, μ_{ext} is set using Eq. (S-37) or (S-38) so that the bulk reservoir occupancy is fixed independent of alloy composition. Subsequent variations in θ_I at grain boundaries or surfaces then arise solely from the local structural and chemical effects encoded in $\Delta f_I(\text{site } j)$, not from an implicit shift of the reservoir.

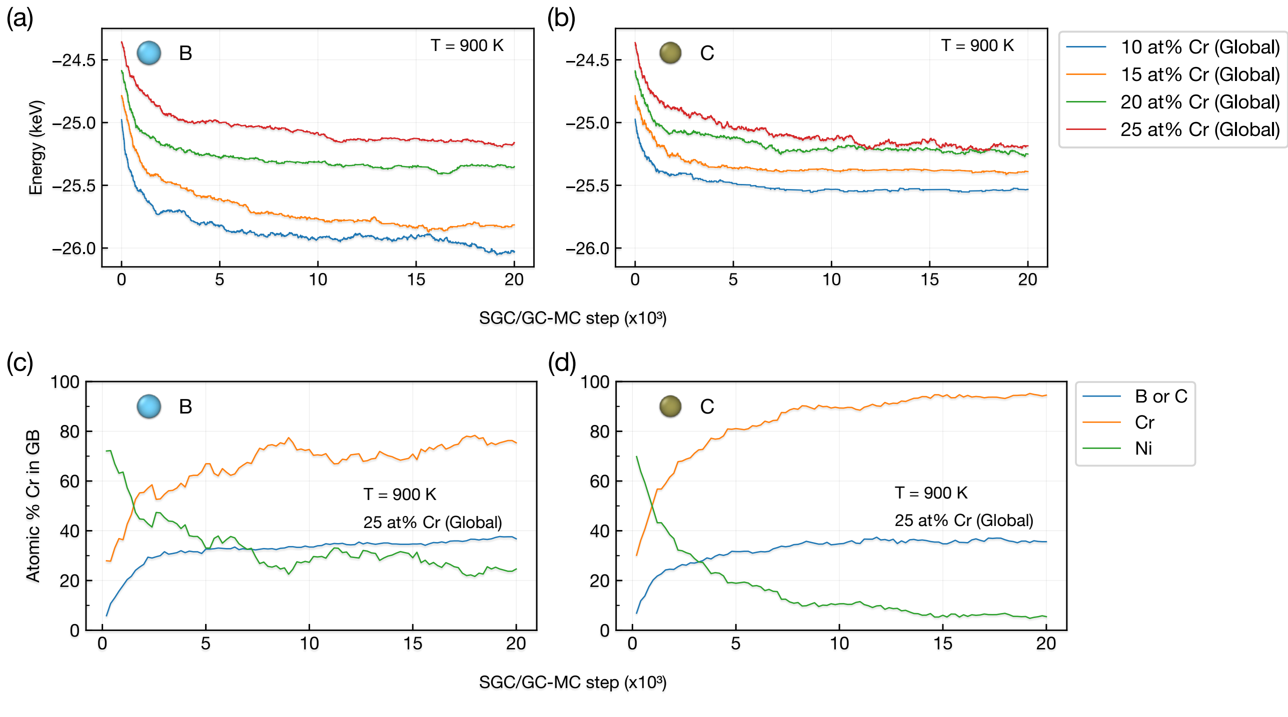

Figure S5: Convergence curves for the $\Sigma 5\,[001]\,(210)$ grain boundary. Total energy versus Monte Carlo step at T = 900 K for (a) boron and (b) carbon. Grain boundary composition as a function of Monte Carlo step at T = 900 K with a global Cr reservoir of 25 at.% for (c) boron and (d) carbon.

5 SGC/GC-MC Convergence Curves

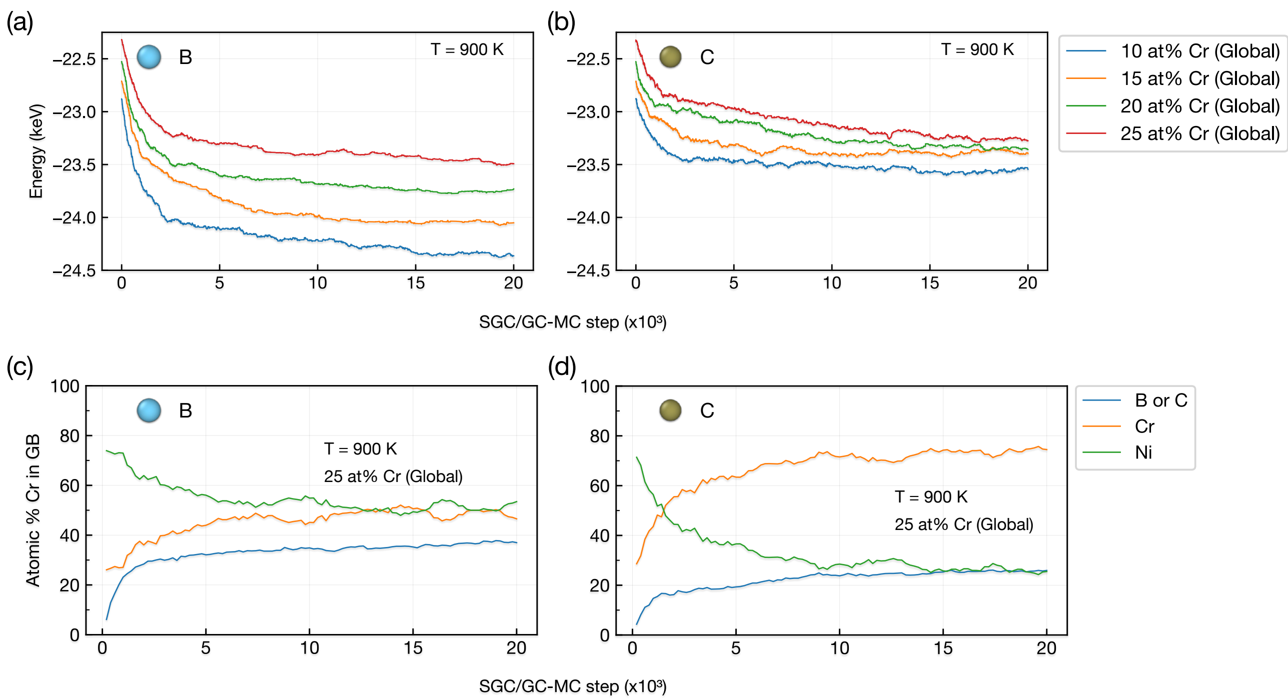

Figure S6: Convergence curves for the high-angle grain boundary. Total energy versus Monte Carlo step at T = 900 K for (a) boron and (b) carbon. Grain boundary composition as a function of Monte Carlo step at T = 900 K with a global Cr reservoir of 25 at.% for (c) boron and (d) carbon.

6 State Variable Values

System	T (K)	x_{Cr} (at.%)	S5				HA			
			$\tilde{\Omega}_{\mathrm{ex}}$	Γ_{I}	Γ_{Cr}	w	$\tilde{\Omega}_{\mathrm{ex}}$	Γ_{I}	Γ_{Cr}	w
B	300	10	-1.227	0.119	-0.061	4.400	-1.166	0.210	-0.069	8.281
		15	-1.728	0.099	-0.037	3.937	-1.549	0.173	-0.085	7.086
		20	-2.905	0.088	0.017	3.585	-2.535	0.156	-0.043	6.790
		25	-4.238	0.076	0.087	3.108	-3.766	0.152	0.060	7.005
	600	10	-1.145	0.120	-0.047	5.290	-1.167	0.224	-0.089	8.525
		15	-1.791	0.114	-0.061	4.932	-1.495	0.189	-0.069	7.981
		20	-2.748	0.099	0.003	4.616	-2.423	0.166	-0.091	7.182
		25	-4.070	0.114	0.073	5.162	-3.610	0.163	0.064	7.666
	900	10	-0.831	0.165	-0.052	7.278	-0.883	0.246	-0.083	9.503
		15	-1.347	0.146	-0.073	6.623	-1.326	0.209	-0.104	8.867
		20	-2.476	0.101	0.011	4.902	-2.138	0.193	-0.036	8.606
		25	-3.656	0.122	0.095	5.625	-3.198	0.194	0.034	8.441
	1200	10	-0.500	0.192	-0.075	9.450	-0.589	0.232	-0.081	10.367
		15	-1.033	0.172	-0.079	8.522	-0.843	0.219	-0.103	10.395
		20	-1.877	0.112	-0.001	6.326	-1.670	0.223	-0.065	10.339
		25	-3.086	0.163	0.067	7.573	-2.492	0.191	0.046	9.164
C	300	10	-0.619	0.071	0.022	3.801	-0.393	0.075	0.011	5.961
		15	-1.269	0.073	0.054	3.814	-1.031	0.079	0.056	5.597
		20	-2.511	0.082	0.154	3.728	-2.201	0.109	0.145	6.958
		25	-4.073	0.115	0.186	4.913	-3.573	0.113	0.179	7.375
	600	10	-0.415	0.073	0.057	4.148	-0.340	0.087	0.011	6.887
		15	-1.194	0.074	0.058	4.009	-0.880	0.095	0.058	6.815
		20	-2.370	0.093	0.174	4.315	-2.072	0.118	0.155	7.642
		25	-3.912	0.118	0.177	5.129	-3.560	0.154	0.229	8.809
	900	10	-0.273	0.074	0.053	4.306	0.006	0.093	0.012	7.428
		15	-0.929	0.076	0.066	4.190	-0.559	0.097	0.068	7.625
		20	-2.132	0.096	0.153	4.633	-1.822	0.130	0.158	8.281
		25	-3.486	0.126	0.177	5.716	-3.161	0.157	0.219	9.216
	1200	10	0.047	0.074	0.016	5.856	0.338	0.096	-0.010	8.558
		15	-0.363	0.079	0.078	5.116	-0.253	0.106	0.042	8.712
		20	-1.411	0.096	0.132	5.422	-1.157	0.132	0.122	9.455
		25	-2.693	0.140	0.187	7.075	-2.286	0.139	0.169	9.450

Table S4: Grand potential excess energies ($\tilde{\Omega}_{\mathrm{ex}}$), Gibbsian interfacial excesses of interstitial (Γ_{I}, I = B or C) and substitutional Cr (Γ_{Cr}), and effective grain boundary widths (w) for the $\Sigma5\,[001]\,(210)$ symmetric tilt (S5) and high-angle (HA) grain boundaries. Values are reported as a function of temperature (T) and bulk Cr fraction (x_{Cr}). $\tilde{\Omega}_{\mathrm{ex}}$ is reported in J/m^2, interfacial excesses are given in atoms/Å^2, and widths in Å. These are the mean values extracted from the final 25 ps of the corresponding MD trajectories.

7 Spectral Analysis

To quantify trends in site-resolved spectral distributions, we analyze each discrete set of spectral values $\{X_i\}_{i=1}^N$, where X may represent segregation energies (E_{seg}) or local chemical ordering metrics (e.g., pairwise short-range order parameters), using a kernel density estimate (KDE) to obtain a continuous probability density function (PDF) $p(X)$. Specifically, we construct

$$p(X) = \frac{1}{Nh} \sum_{i=1}^{N} K\left(\frac{X - X_i}{h}\right), \tag{S-39}$$

where $K(\cdot)$ is a Gaussian kernel and h is the bandwidth. The KDE is evaluated on a uniform grid $X \in [X_{\min} - \Delta,\, X_{\max} + \Delta]$ and normalized to satisfy

$$\int_{-\infty}^{\infty} p(X)\, dX \approx \int p(X)\, dX = 1, \tag{S-40}$$

where the integral is computed numerically using trapezoidal integration on the discrete grid.

Using $p(X)$ and the underlying samples, we compute three spectral descriptors, reported in Fig. S7.

Weighted average spectral value. We compute the mean value associated with each spectrum as the first moment of the PDF,

$$\langle X \rangle = \int X\, p(X)\, dX, \tag{S-41}$$

evaluated numerically on the KDE grid. This quantity provides a single-valued descriptor of the central tendency of the spectrum.

Spectral width via interquartile range (IQR). We quantify the spread of each spectrum using the interquartile range,

$$\mathrm{IQR} = Q_{0.75} - Q_{0.25}, \tag{S-42}$$

where Q_q denotes the qth percentile of the discrete $\{X_i\}$ distribution. The IQR provides a robust measure of spectral width that is insensitive to extreme tails.

Fraction of strongly favorable or ordered environments. To quantify the spectral weight residing in the strongly favorable or strongly ordered tail of the distribution, we compute the integrated probability mass below a threshold value X^*,

$$f_{\mathrm{strong}}(X^*) = \int_{-\infty}^{X^*} p(X)\, dX. \tag{S-43}$$

The threshold X^* is chosen based on the physical interpretation of the spectrum under consideration. In the present work, we use $X^* = -2.0$ eV for segregation-energy spectra to identify strongly favorable segregation sites, and $X^* = -1.0$ for local SRO spectra to identify strongly ordered solute–solute environments. The quantity f_{strong} is evaluated numerically by integrating the KDE-PDF over $X \leq X^*$.

Segregation Energy

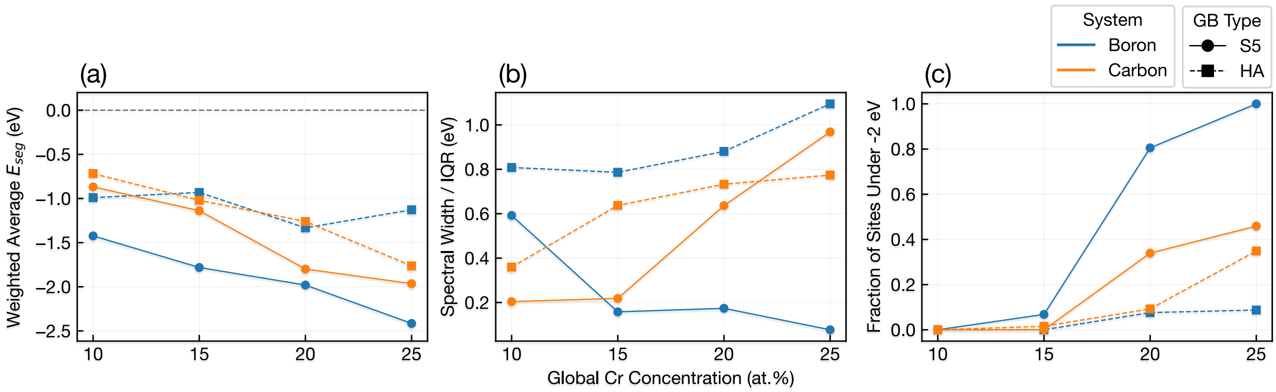

Figure S7: Metrics extracted from the site-resolved segregation energy distributions at 300 K for boron and carbon at the S5 and HA grain boundaries as a function of global Cr concentration. (a) Weighted average segregation energy. (b) Spectral width quantified by the interquartile range (IQR). (c) Fraction of highly favorable segregation environments, defined as the integrated probability mass of the KDE spectrum for $E_{\text{seg}} \leq -2.0$ eV. These metrics provide quantitative support for trends inferred from the full segregation spectra shown in the main text.

As a reminder, segregation energy is defined as,

$$E_{\text{seg}}^{(I)} = E_{\text{GB}}^{I@\text{GB}} - \langle E_{\text{GB}}^{I@\text{bulk}} \rangle \tag{S-44}$$

where $E_{\text{GB}}^{I@\text{GB}}$ is the total energy of the system with an interstitial occupying a grain boundary void site, and $\langle E_{\text{GB}}^{I@\text{bulk}} \rangle$ is the total energy of the system with the interstitial placed in an octahedral site within the bulk region of the same simulation cell. The angular brackets denote averaging over multiple bulk sites, which accounts for local variations in Cr content within the first nearest-neighbor coordination shell of each octahedral cage. Negative $E_{\text{seg}}^{(I)}$ values indicate energetically favorable segregation to the grain boundary, while positive values indicate preference for bulk occupancy.

The quantitative spectral descriptors shown in Fig. S7 provide additional resolution of the segregation behavior discussed in the main text. For the S5 boundary (blue circle markers), the weighted average boron segregation energy decreases monotonically with increasing global Cr concentration, with the Cr-rich structure corresponding to the most favorable average segregation state. This trend is accompanied by a sharp reduction in spectral width, reflecting the progressive loss of energetically favorable void sites other than the central void. Despite this loss of accessible sites, the fraction of strongly favorable sites increases markedly, as the remaining central void environments correspond to deep segregation wells, all of which fall below the -2.0 eV threshold.

For carbon at the S5 boundary (orange circle markers), the weighted average segregation energy also decreases continuously with increasing Cr content, although it remains less negative than that of boron across all compositions. In contrast to boron, this stabilization is accompanied by significant spectral widening, consistent with the increasing heterogeneity of the interfacial energy landscape described in the main text. The fraction of strongly favorable sites likewise increases with Cr content, indicating that carbon gains access to an expanding population of deep insertion environments in the Cr-rich regime.

At the HA boundary, boron exhibits qualitatively different behavior (blue square markers). Unlike the S5 case, no clear monotonic decrease in the average segregation energy is observed as the global Cr concentration approaches 25 at.%. Across all compositions, boron segregation energies at the HA boundary are less negative than their S5 counterparts. The spectral width remains comparatively stable with increasing x_{Cr}, with a noticeable increase at 25 at.% Cr corresponding to the Ni–Cr mixed configuration. Although the HA spectra are consistently broader than those of the S5 boundary, the fraction of strongly favorable boron sites remains low, reaching a maximum of approximately 10% in the Ni–Cr mixed structure.

Carbon segregation at the HA boundary (orange square markers) shows a continuous decrease in the weighted average segregation energy with increasing Cr content, again remaining less negative than in the corresponding S5 structures. The spectral width increases with Cr concentration and appears to asymptote near ~ 0.8 eV, with a maximum at 25 at.% Cr that remains smaller than the corresponding S5 spectral width. The fraction of strongly favorable sites increases more gradually than in the S5 boundary and does not exceed the S5 values, reaching a maximum of approximately 35% in the Cr-rich HA structure.

Local Short-range Order

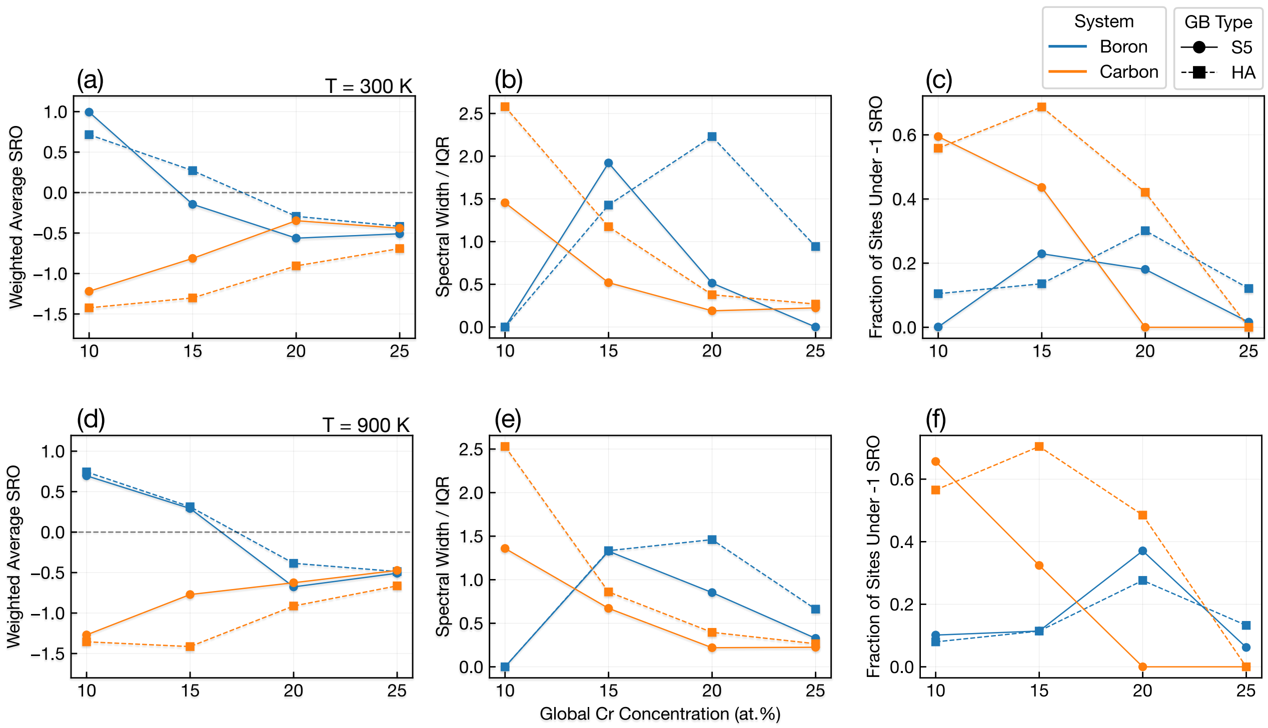

Figure S8: Metrics extracted from the site-resolved Warren–Cowley short-range order (SRO) distributions at (a-c) 300 K and (d-f) 900 K for boron and carbon at the S5 and high-angle (HA) grain boundaries as a function of global Cr concentration. (a,d) Weighted average SRO. (b,e) Spectral width quantified by the interquartile range (IQR). (c,f) Fraction of strongly ordered environments, defined as the integrated probability mass of the KDE spectrum for $\alpha \leq -1.0$.

The SRO spectral analysis reveals fundamentally different ordering responses for boron and carbon as a function of global Cr concentration, reflecting their distinct interactions with the evolving grain boundary chemical environment. At low Cr contents, the grain boundaries remain predominantly Ni-rich, and boron exhibits largely positive B–Cr SRO values, indicating weak or unfavorable local association with Cr. As the global Cr concentration increases toward 20 at.%, the grain boundary chemistry transitions to a mixed Ni–Cr environment, enabling modestly favorable B–Cr ordering. This transition is reflected in the weighted-average B–Cr SRO becoming negative, stabilizing at approximately $\alpha \approx -0.5$ by 20 at.% Cr and persisting to 25 at.% for both 300 K and 900 K in the S5 and high-angle grain boundaries.

At 25 at.% Cr in the S5 boundary, the B–Cr SRO spectrum becomes extremely narrow, with an interquartile range approaching zero. This collapse of spectral width reflects the reduction of accessible boron segregation sites to a single dominant chemical motif associated with the central void site, such that boron effectively samples only one local environment. Consistent with this interpretation, the excess Cr concentration at the grain boundary, Γ_{Cr}, continues to increase with global Cr content in the boron-doped structures, indicating that the observed narrowing arises from site exhaustion rather than diminished Cr availability. The fraction of strongly ordered B–Cr environments increases at intermediate Cr concentrations (15 at.%) but decreases steadily toward 25 at.% at 300 K, while at 900 K the strongly ordered fraction peaks near 20 at.% before declining. A similar decrease at 25 at.% is observed for the high-angle boundary at both temperatures, indicating that increased exposure to Cr produces a more uniform distribution of B–Cr ordering rather than increasingly extreme local motifs.

Carbon exhibits a markedly different response. At low Cr concentrations, the C–Cr SRO spectra are broad, with interquartile ranges approaching IQR ≈ 1.5 and spanning both positive and negative α values. Despite this heterogeneity, the weighted-average C–Cr SRO is strongly negative ($\alpha \approx -1.25$), indicating a strong intrinsic preference for Cr-rich local environments even in Ni-dominated boundaries. Unlike boron, the average C–Cr SRO becomes less negative with increasing Cr concentration, asymptotically approaching $\alpha \approx -0.5$. In the S5 boundary, boron and carbon converge to nearly identical average SRO values at both 300 K and 900 K, whereas in the high-angle boundary carbon maintains more negative C–Cr ordering than boron at all compositions and temperatures examined.

At both temperatures, the spectral width of the C–Cr ordering progressively narrows with increasing Cr concentration, approaching IQR ≈ 0.25 in both grain boundary structures. The fraction of strongly ordered C–Cr environments decreases correspondingly at both 300 K and 900 K. In the S5 boundary, this decay occurs rapidly with increasing Cr content, whereas in the high-angle boundary the strongly ordered fraction initially increases at 15 at.% Cr before decreasing steadily toward 25 at.%, ultimately reaching zero in a manner similar to boron. Together, these trends indicate that while carbon initially accesses a wide population of chemically distinct Cr-rich environments, increasing Cr content homogenizes the available local motifs, reducing both chemical heterogeneity and the prevalence of extreme ordering environments.

The broad C–Cr SRO spectra observed at 10 at.% Cr arise from a combination of chemical scarcity and sampling heterogeneity in the Ni-rich grain boundary environment. At this composition, the grain boundary slab contains relatively few Cr atoms and a limited number of interfacial carbon atoms, such that individual carbon sites experience highly variable local Cr coordination. As a result, the conditional probability $P_{(\mathrm{Cr}|\mathrm{C})}$ becomes sensitive to discrete changes in neighbor count, and local SRO values span both positive and negative α regimes depending on whether a given carbon atom is adjacent to zero, one, or multiple Cr neighbors. This produces a wide SRO spectrum with a large interquartile range in both the S5 and high-angle grain boundaries.

As the global Cr concentration increases, the grain boundary transitions from a Ni-rich to mixed Ni–Cr, to Cr-rich chemical environment, accompanied by increased carbon incorporation at the interface. In this regime, carbon atoms encounter a higher and more uniform probability of Cr neighbors, increasing the prevalence of C–Cr bonds and reducing site-to-site variability in $P_{(\mathrm{Cr}|\mathrm{C})}$. Consequently, the distribution of local SRO values narrows and asymptotically converges toward a well-defined mean, reflected in the systematic reduction of the spectral width at both 300 K and 900 K. This collapse of the C–Cr SRO spectrum indicates that increasing Cr availability homogenizes the chemical motifs accessible to carbon, suppressing extreme local ordering environments and yielding a more uniform interfacial chemical state.

The opposite evolution of the C–Cr and B–Cr SRO values with increasing global Cr concentration reflects fundamentally different population responses of carbon and boron within the grain boundary region. For carbon, increasing x_{Cr} leads to a concurrent increase in both Cr and C atom counts within the grain boundary slab. As a result, the reference solute fraction c_{Cr} increases alongside the conditional probability $P_{(\mathrm{Cr}|\mathrm{C})}$, such that the ratio $P_{(\mathrm{Cr}|\mathrm{C})}/c_{\mathrm{Cr}}$ approaches unity. This drives the SRO parameter toward less negative values, even though the absolute number of C–Cr bonds increases. In this regime, carbon continues to associate with Cr-rich environments, but the environments themselves become increasingly representative of the average boundary chemistry, reducing the apparent strength of ordering relative to a random reference state.

Boron exhibits the opposite trend. As x_{Cr} increases, the Cr content of the grain boundary rises, but the number of accessible boron sites decreases due to site exhaustion and increased competition with Cr-rich motifs. Consequently, boron becomes increasingly confined to a small subset of Cr-rich environments, such that $P_{(\mathrm{Cr}|\mathrm{B})}$ increases relative to the rising background concentration x_{Cr}. This selective sampling of Cr-enriched sites drives the B–Cr SRO to more negative values with increasing x_{Cr}, even as the total number of boron atoms in the boundary decreases.

Together, these opposing trends highlight a key distinction between carbon and boron at grain boundaries: carbon responds to increasing Cr content by homogenizing across an expanding population of Cr-bearing environments, whereas boron responds by localizing into a shrinking subset of highly Cr-enriched sites. The resulting divergence in SRO evolution underscores the different mechanisms by which carbon conditions the boundary chemistry and boron subsequently stabilizes specific interfacial motifs.

An additional trend is that both B–Ni and C–Ni SRO values become increasingly positive with increasing x_{Cr}, consistent with progressive replacement of Ni neighbors by Cr within the grain boundary coordination network. For carbon, this behavior is expected given its strong co-segregation tendency with Cr-bearing interfacial environments. For boron, however, the evolution reflects a crossover between two regimes. At low x_{Cr} (10–15 at.%), the boundary remains Ni-rich and boron preferentially occupies structurally favorable motifs that are predominantly Ni-coordinated; in this regime, boron can locally suppress Cr adjacency and the limited Cr population is readily displaced to other boundary regions or the bulk. As x_{Cr} increases (20–25 at.%), the Cr chemical reservoir at the interface grows and Cr-rich motifs become pervasive, eliminating boron's ability to exclude Cr from its local environment. Boron instead localizes into the remaining Cr-tolerant segregation motifs (notably the dominant void-associated site in the S5 boundary), yielding increasingly negative B–Cr SRO and correspondingly more positive B–Ni SRO. Thus, the apparent reversal from Cr depletion at low x_{Cr} to Cr preference at high x_{Cr} reflects a transition from boron-controlled motif selection in a Ni-rich boundary to reservoir-controlled chemical conditioning in a Cr-rich boundary.

8 Validation of the PreFerred Potential

Atomic Pair	**MP ID**	**DFT μ_I (eV/atom)**	**PFP μ_I (eV/atom)**
Cr–B	mp-1080664	−7.738	−7.419
Mo–B	mp-1890	−7.684	−7.525
Ti–B	mp-1145	−8.263	−8.254
Cr–C	mp-723	−9.573	−8.604
Mo–C	mp-1552	−9.566	−8.380
Ti–C	mp-10721	−11.158	−9.963
Cr–H	mp-24208	−3.452	−2.380
Mo–H	mp-24417	−2.426	−1.355
Ti–H	mp-24726	−4.118	−3.127
Cr–N	mp-8780	−9.494	−6.118
Mo–N	mp-2811	−9.070	−6.122
Ti–N	mp-492	−11.770	−9.509

Table S5: Interstitial chemical potential energies derived from DFT and the PreFerred Potential (PFP), based on total energies of selected binary compounds. Values are given in eV per interstitial atom. Results compiled from Ref. [5].

Metric	PFP Prediction	DFT Benchmark	Comment
Ni→Cr substitution energy	-0.343 eV	-0.732 eV	Both predict exothermic mixing (108 atoms)
$\Delta\mu$(**B−C**)	-1.559 eV	-2.600 eV	Both predict C more stable than B
Ni_2B E_{form}	-4.008 eV	-3.392 eV	Both predict stable
Ni_3C E_{form}	+1.324 eV	+2.016 eV	Both predict unstable
GB energy (Σ5 in Ni)	1.20 J/m^2	1.29 J/m^2 [6]	PFP value is size-converged
B diffusion in FCC Ni	1.48 eV	1.77 eV [7]	PFP value is size-converged
B diffusion in Ni with one Mo neighbor	2.20 eV	2.74 eV [7]	Mo coordination raises barrier; PFP value is size-converged
$E_{\text{seg}}^{\text{boron}}$ **to Σ5 GB in Ni**	−1.50 eV	−2.00 eV [8]	PFP value is size-converged (bulk and GB)
SRO: N–Cr	Negative 1NN SRO [5]	Same trend [9]	Fig. 3a shows agreement
SRO: N–Ni	Positive 1NN SRO [5]	Same trend [9]	Fig. 3a shows agreement
SRO: Fe–Cr	Negative 1NN SRO (this work)	Same trend [9]	Fig. 4a shows agreement
SRO: Ni–Cr	Negative 1NN SRO [5]	Same trend [9]	Fig. 4b shows agreement

Table S6: Comparison between PreFerred Potential (PFP) and DFT predictions across various thermodynamic and diffusion metrics. Size convergence refers to the simulation cell size used to compute each value. Nitrogen SRO comparisons use our prior work (Ref. [5]) as the PFP benchmark. Comments refer to the corresponding DFT benchmarks, including figures from the cited sources. Substitution energy for Cr into Ni was computed using the PBE exchange-correlation functional within VASP.

Table S6 validates the PFP against DFT across a comprehensive range of properties relevant to this study. PFP quantitatively reproduces DFT energetics with typical deviations of 7-34%, including grain boundary energies, diffusion barriers, and formation energies. Critically, PFP preserves all qualitative trends: compound stability signs (Ni_3B stable, Ni_3C unstable), chemical potential ordering (C more stable than B), and short-range ordering tendencies for multiple solute pairs. This agreement across energetic, kinetic, and structural properties demonstrates that PFP captures the essential physics governing solute behavior in Ni-based alloys, providing confidence that phase diagrams and segregation trends predicted by PFP-driven SGC/GC-MC simulations reflect DFT predictions in their qualitative features and semi-quantitative energetics.

References

[1] A. Stukowski, "Visualization and analysis of atomistic simulation data with OVITO–the Open Visualization Tool," *Modelling and Simulation in Materials Science and Engineering*, vol. 18, p. 015012, Dec. 2009.

[2] P. Hirel, "Atomsk: A tool for manipulating and converting atomic data files," *Computer Physics Communications*, vol. 197, pp. 212–219, Dec. 2015.

[3] A. P. Thompson, H. M. Aktulga, R. Berger, D. S. Bolintineanu, W. M. Brown, P. S. Crozier, P. J. Veld, A. Kohlmeyer, S. G. Moore, T. D. Nguyen, R. Shan, M. J. Stevens, J. Tranchida, C. Trott, and S. J. Plimpton, "LAMMPS - a flexible simulation tool for particle-based materials modeling at the atomic, meso, and continuum scales," *Computer Physics Communications*, vol. 271, p. 108171, Feb. 2022.

[4] N. Tso, M. Kosugi, and J. Sanchez, "The effect of the structural energy of Cr on the Ni-Cr equilibrium phase diagram," *Acta Metallurgica*, vol. 37, pp. 121–127, Jan. 1989.

[5] T. D. Doležal, R. Freitas, and J. Li, "Segregation and ordering of light interstitials (B, C, H, and N) in Cr-Ni alloys: Implications for grain boundary stability in superalloy design," *Acta Materialia*, p. 121221, 2025.

[6] D. Di Stefano, M. Mrovec, and C. Elsässer, "First-principles investigation of hydrogen trapping and diffusion at grain boundaries in nickel," *Acta Materialia*, vol. 98, pp. 306–312, Oct. 2015.

[7] J. Y. Ji, Z. Zhang, J. Chen, H. Zhang, Y. Z. Zhang, and H. Lu, "Effect of refractory elements M (=Re, W, Mo or Ta) on the diffusion properties of boron in nickel-based single crystal superalloys," *Vacuum*, vol. 211, p. 111923, May 2023.

[8] Y. Chen, H. Yu, H. Di, and W. Xu, "Enhancing sulfur embrittlement resistance in Ni-based superalloys through synergistic effects of boron and carbon co-doping," *Journal of Materials Science*, vol. 60, pp. 445–462, Jan. 2025.

[9] T. Su, B. J. Blankenau, N. Kim, J. A. Krogstad, and E. Ertekin, "Nitrogen-related short-range order in Fe-Ni-Cr austenitic stainless steels: First principles and cluster expansion study," July 2025.